



Nanoscale  
Horizons

**Analytical van der Waals interaction potential for faceted nanoparticles**

Journal:	<i>Nanoscale Horizons</i>
Manuscript ID	NH-COM-09-2020-000526.R1
Article Type:	Communication
Date Submitted by the Author:	22-Oct-2020
Complete List of Authors:	Lee, Brian; Duke University, Mechanical Engineering and Materials Science Arya, Gaurav; Duke University, Mechanical Engineering & Materials Science; Duke University

SCHOLARONE™  
Manuscripts

## **New Concept Statement**

There is tremendous interest in understanding the interaction forces acting between faceted nanoparticles because of their ability to self-assemble into novel higher-order architectures with unique optical and mechanical properties. One of the most fundamental components of such interactions acting between nanoparticles is the van der Waals (vdW) forces. While vdW forces can be rapidly calculated using analytical models for simple and symmetric particle geometries, no such models exist for faceted particles. In this work, we develop the first analytical model for the vdW interaction potential between faceted nanoparticles. The model was derived by reducing the usual six-dimensional integral over particle volumes to a series of two-dimensional integrals over particle interaction areas with closed-form solutions. The model can accurately capture the vdW energy landscape of diverse particle shapes, while yielding many orders of magnitude improvement in computational efficiency compared to brute-force atomistic calculations. The model's accuracy, efficiency, and ease of implementation will allow researchers to rapidly explore vdW energy landscapes of faceted nanoparticles and enable many future investigations on the rheology, phase behavior, and self-assembly of such particles through simulations that have so far been impeded by the prohibitive costs of accurately evaluating vdW energies.

# **Analytical van der Waals interaction potential for faceted nanoparticles**

Brian Hyun-jong Lee and Gaurav Arya\*

*Department of Mechanical Engineering and Materials Science,  
Duke University, Durham, NC 27708, USA*

E-mail: [gaurav.arya@duke.edu](mailto:gaurav.arya@duke.edu)

Phone: +1 (919) 660-5435. Fax: +1 (919) 660-8963

### Abstract

Our ability to synthesize faceted nanoparticles of tunable shapes and sizes has opened up many intriguing applications of such particles. However, our progress in understanding, modeling, and simulating their collective rheology, phase behavior, and self-assembly has been hindered by the lack of analytical interparticle interaction potentials. Here, we present one of the first analytical models for the van der Waals interaction energy between faceted nanoparticles. The model was derived through various approximations that reduce the usual six-dimensional integral over particle volumes to a series of two-dimensional integrals over particle interaction areas with closed-form solutions. Comparison and analyses of energies obtained from the analytical model with those computed from exact atomistic calculations show that the model approximations lead to insignificant errors in predicted energies across all relevant particle configurations. We demonstrate that the model yields accurate energies for diverse particle shapes including nanocubes, triangular prisms, faceted rods, and square pyramids, while yielding many orders of magnitude improvement in computational efficiency compared to atomistic calculations. To make the model more accessible and to demonstrate its applicability, an open-source graphical user interface application implementing the model for nanocubes in arbitrary configurations has been developed. We expect that the analytical model will accelerate future investigations of faceted nanoparticles that require accurate calculation of interparticle interactions.

## INTRODUCTION

Advancements in solution-based synthesis techniques have enabled researchers to produce faceted nanoparticles (NPs) of various shapes and sizes.<sup>1,2</sup> Because of their sharp edges and flat surfaces, faceted NPs exhibit useful properties such as enhanced catalytic activity,<sup>3,4</sup> improved cellular uptake,<sup>5-7</sup> and unusual plasmonic resonances.<sup>8,9</sup> In addition, faceted NPs can be used as building blocks for assembly of particle clusters and superlattices with new and complex arrangements that cannot be achieved by spherical NPs. Such assembled states of NPs could have potential applications in plasmonics,<sup>10-12</sup> metamaterials,<sup>13-15</sup> chiroptical sensors,<sup>16,17</sup> photovoltaics,<sup>18,19</sup> and quantum-dot solids.<sup>20,21</sup> A key quantity that determines the morphology of structures formed by NPs is their pairwise interaction potential energy, and one of the most fundamental component of interparticle interactions is the van der Waals (vdW) forces. These forces are almost always attractive and arise from the dipole-dipole interactions acting between atoms across NPs. In general, vdW forces encompass not only interactions between instantaneous dipoles and induced dipoles, but also interactions between permanent dipoles and between permanent dipoles and induced dipoles. In some definitions, vdW forces also include the short-range repulsion arising from Pauli exclusion principle, which prevents atoms and particles from overlapping. Though vdW interactions are much weaker than covalent, ionic, or metallic bonds and typically have a shorter range than charge-charge interactions, they are ubiquitous as they act across all atomic species. As a result, the collective vdW interactions between NPs can become substantial ( $\gg$  thermal energy  $k_B T$ ) and are often the main driving force for particle assembly and aggregation.

A common approach for calculating the vdW interaction energy  $U_{\text{vdW}}$  between two NPs involves summing up vdW energies contributed by all pairs of atoms interacting across the two particles, as given by  $U_{\text{vdW}} = \sum_{i=1}^N \sum_{j=1}^N U_{\text{LJ}}(r_{ij})$ . Here,  $r_{ij}$  is the distance between atoms  $i$  and  $j$  on separate NPs and  $N$  is the number of atoms in each NP, assumed to be identical here. The pairwise interactions are usually treated using the Lennard-Jones (LJ) potential  $U_{\text{LJ}} = 4\varepsilon[(\sigma/r)^{12} - (\sigma/r)^6]$ , in which  $\sigma$  represents the atomic size, the first term

accounts for the attractive vdW interactions due to dipoles, and the second term empirically models the electron-electron repulsion due to Pauli exclusion principle. The interaction energy parameter  $\varepsilon$  can be related to the Hamaker constant obtained from experiments<sup>22,23</sup> or from Lifshitz theory.<sup>24</sup> While such “atomistic summation” approach does not properly account for retardation and many-body effects, it provides a straightforward means to calculating vdW interactions between NPs of arbitrary shapes. However, because NPs contain many atoms ( $N \sim 10^4$  to  $10^8$ ) and each vdW energy calculation requires  $\mathcal{O}(N^2)$  LJ energy evaluations, this approach becomes computationally expensive for exploring energy landscapes of NPs, where energy needs to be computed as a function of particle position and orientation, and prohibitive for simulations, where interactions between NPs need to be computed over hundreds of particles and millions of time steps. For this reason, researchers have attempted to obtain analytical solutions to  $U_{\text{vdW}}$  by replacing the summation over interatomic LJ interactions with an integral of the LJ potential over the volumes  $V_1$  and  $V_2$  of the interacting NPs, that is,  $U_{\text{vdW}} \approx \rho^2 \int_{V_1} \int_{V_2} U_{\text{LJ}}(r_{ij}) dV_1 dV_2$ , where  $\rho$  is the number density of atoms in the NPs.<sup>25</sup> For spherical particles, this integral can be solved exactly by taking advantage of the geometric symmetry of the particles.<sup>26</sup> Analytic solutions also exist for other simple and symmetric shapes such as spherical shells, parallel flat surfaces, and parallel cylinders in close proximity.<sup>25,27</sup> However, no such closed-form solutions exist for vdW interactions between faceted NPs whose asymmetric shape and finite span along each dimension render the above integral analytically intractable.

Because of the lack of analytic expressions for vdW interactions between faceted NPs, simulation studies using accurate descriptions of  $U_{\text{vdW}}$  via atomistic summation have been limited to small system sizes.<sup>28,29</sup> For larger systems, researchers have resorted to approximate descriptions of  $U_{\text{vdW}}$  to reduce the computational cost. For instance, the NPs could be constructed out of much fewer coarse beads, each intended to represent a large group of atoms.<sup>30,31</sup> However, the vdW energy, including its distance and orientational dependence, obtained by summing over interbead LJ interactions across the NPs can differ significantly

from that obtained from atomistic summation. In many cases, researchers choose to neglect attractive vdW interactions altogether,<sup>32–36</sup> retaining only the excluded-volume interactions, which can be more efficiently implemented by using algorithms that check for geometric overlaps between NPs<sup>37,38</sup> or by representing NPs using shells of short-range repulsive beads.<sup>39,40</sup> While approximating or neglecting vdW interactions between particles may be acceptable for exploring granular packing in macroscopic particles or for studying entropy-driven crystallization of NPs, a proper and accurate description of vdW interactions between faceted NPs is necessary for studying their self-assembly and phase behavior, as evident from past work on spherical NPs.<sup>41–45</sup> Hence, there is tremendous interest in accurately and efficiently accounting for vdW interactions in studies involving faceted NPs.

Here we present the first analytical model for calculating the vdW interactions energy between faceted NPs. The model was achieved by discretizing the volume of one of the NPs into parallel rods and deriving a simplified potential for the vdW interactions between a rod and a NP, allowing us to convert the usual vdW integral of interatomic potential over particle volumes into a series of analytically solvable area integrals of the rod-NP potential over the interacting facets of the NP. The resulting expressions are able to accurately describe the full vdW energy landscape for a range of faceted NPs, including cubes, triangular prisms, faceted rods, and square pyramids. The analytical model can be easily coded into computational routines, and as demonstration we provide an open-source graphical user interface application for calculating the vdW energy of nanocubes in arbitrary configurations. The accuracy and computational efficiency of the analytical model developed here should enable a range of simulation studies on the rheology, self-assembly, and phase behavior of faceted NPs, previously found to be computationally prohibitive.

## RESULTS

**Model Development.** Our approach for deriving analytical vdW potentials for faceted particle, using nanocubes as the example, is summarized in Fig. 1. Given two NPs in

arbitrary orientations (Fig. 1a), we first transform the coordinate frame of reference so that one particle (P1) is at the origin with one of its faces denoted by  $\mathcal{F}_1$  oriented perpendicular to the  $x$ -axis as shown in Fig. 1b. The configuration  $\mathbf{R}$  of this two-particle system is then fully described by the position vector and orientation of the other particle (P2). Next, we discretize the volume of P2 into a collection of parallel rod elements oriented normal to the interacting face of P1 as depicted in Fig. 1c. (Henceforth, we use the term “interacting face” to refer to all facets of P1 and P2 that face each other.) The rods are characterized by their length  $b_x$ , separation distance  $d_x$  from P1, and lateral position in the  $y$  and  $z$  directions. The rod separation distance and length are both functions of their lateral position and particle configuration, that is,  $d_x \equiv d_x(y, z; \mathbf{R})$  and  $b_x \equiv b_x(y, z; \mathbf{R})$ .

Consider now that each rod has a cross-section so small that it contains a single line of atoms of size  $\sigma$ . If the vdW interaction energy between a rod and P1 can be described by an interaction potential  $U_{\text{rod}} \equiv U_{\text{rod}}(y, z, d_x, b_x)$ , then the total vdW energy of interaction  $U_{\text{vdW}} \equiv U_{\text{vdW}}(\mathbf{R})$  between the two particles can be written as an area integral of this potential over the entire projected area of P2 (onto the  $y$ - $z$  plane) denoted by  $\mathcal{A}_2$ :

$$U_{\text{vdW}} = \gamma \iint_{(y,z) \in \mathcal{A}_2} U_{\text{rod}}(y, z, d_x, b_x) dz dy, \quad (1)$$

where  $\gamma$  is the area density of the rods (equal to  $\sigma^{-2}$  if the rods are arranged in a square lattice). The above integral is however too complex to yield a closed-form solution, as  $U_{\text{rod}}$  is a function of not only  $y$  and  $z$ , but also  $d_x$  and  $b_x$ , which are also both functions of  $y$  and  $z$ . The integration limits, which themselves are functions of  $y$  and  $z$  for most particle configurations, further complicate the process of obtaining an analytical solution.

To obtain an analytical solution for  $U_{\text{vdW}}$ , we simplify the integrand and limits in Eq. 1 through approximations based on observations that are described and justified in more detail later. Briefly, the first observation is that the rods whose  $y$ - $z$  projections fall outside the boundary of  $\mathcal{F}_1$  contribute negligibly to  $U_{\text{vdW}}$ , an effect that arises due to the short-ranged

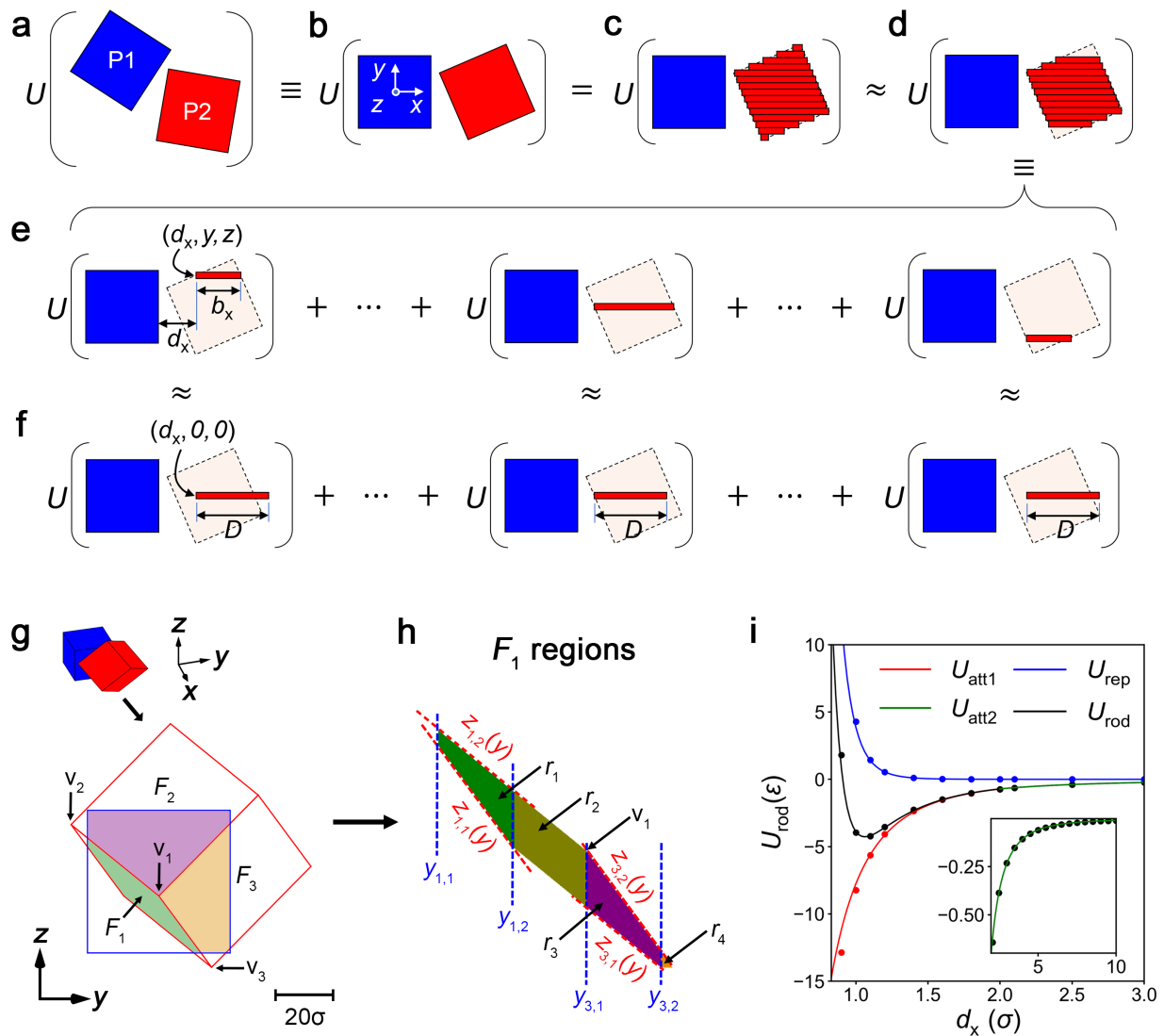


Figure 1: Derivation of analytical vdW potential for faceted NPs. (a) Schematic of cubes P1 and P2 in arbitrary configuration. (b) Coordinate transformation into P1's frame of reference. (c) Segmentation of P2 into rods. (d) Rods outside the  $y$ - $z$  boundaries of P1's interacting face ( $\mathcal{F}_1$ ) are discarded. (e) vdW interaction energy is given by the summation of  $U_{\text{rod}}$ . (f) Each rod is assumed to be of length  $D$  and to be facing the center of  $\mathcal{F}_1$ . In (a)–(f),  $U(\circ)$  denotes potential energy of item  $\circ$ . (g)  $y$ - $z$  projection of  $\mathcal{F}_1$  and the three interacting faces of P2 denoted by  $F_1$ ,  $F_2$ , and  $F_3$ . The three vertices defining the  $F_1$  plane are labeled  $v_1$ – $v_3$ . (h) Segmentation of  $F_1$  into four regions  $r_1$ – $r_4$  in which the  $z$  integral limits can be expressed as linear functions of  $y$ ; integration limits for only  $r_1$  and  $r_3$  are shown for illustration. (i) Power-law fits to the repulsive and attractive portions of the rod potential for  $D = 50\sigma$  nanocubes. Inset shows zoomed view of the long-ranged attraction. Symbols represent energies from atomistic summation and solid lines represent fits.

nature of the interatomic vdW potential. This allows us to discard integration over such rods that fall outside  $\mathcal{F}_1$ 's boundaries (Fig. 1d,e), which simplifies the integration limits in Eq. 1. For instance, both the  $y$  and  $z$  integration limits for nanocubes in the configuration shown in the figure are simply given by  $-D/2$  and  $D/2$ , where  $D$  is the edge length of the cube. The second observation is that the interaction energy  $U_{\text{rod}}$  is insensitive to both the length of the rods beyond a cutoff length smaller than  $D$  and the lateral position of the rods except those outside  $\mathcal{F}_1$ 's boundary. Consequently, the vdW energy contributed by a rod of length  $b_x$  whose P1-proximal end is located at  $(d_x, y, z)$  can be approximated as equal to that of a rod of length  $D$  located at the origin of the  $y$ - $z$  axes,  $(d_x, 0, 0)$  (see Fig. 1f). This then allows us to eliminate  $U_{\text{rod}}$ 's dependency on  $y$ ,  $z$ , and  $b_x$  without much loss in accuracy, making  $U_{\text{rod}}$  solely a function of separation distance  $d_x(y, z)$ . These approximations help convert the original integral in Eq. 1 into a more manageable form:

$$U_{\text{vdW}} = \gamma \iint_{(y,z) \in \mathcal{F}_1} U_{\text{rod}}(d_x(y, z)) dz dy. \quad (2)$$

The last observation is that as in the case of vdW interactions between macroscopic bodies,<sup>25</sup> the attractive and repulsive portions of the rod-NP interaction energy arising from dipole-dipole interactions and Pauli exclusion principle can each be approximated by power-law functions:

$$U_{\text{rod}} = \sum_{\nu} C_{\nu} (\sigma/d_x)^{n_{\nu}}, \quad (3)$$

where  $C_{\nu}$  are constants describing the strengths of each interaction component and  $n_{\nu}$  are exponents that describe how rapidly these components decay with separation distances.

Given that both particles are faceted, the distance  $d_x$  between the two interacting facets is always a linear function of  $y$  and  $z$  as given by

$$d_x = c_1 y + c_2 z + c_3 \quad (4)$$

$$\begin{aligned}
c_1 &= \frac{(x_{v2} - x_{v1})(z_{v3} - z_{v1}) - (z_{v2} - z_{v1})(x_{v3} - x_{v1})}{(y_{v2} - y_{v1})(z_{v3} - z_{v1}) - (z_{v2} - z_{v1})(y_{v3} - y_{v1})}, \\
c_2 &= \frac{(y_{v2} - y_{v1})(x_{v3} - x_{v1}) - (x_{v2} - x_{v1})(y_{v3} - y_{v1})}{(y_{v2} - y_{v1})(z_{v3} - z_{v1}) - (z_{v2} - z_{v1})(y_{v3} - y_{v1})}, \\
c_3 &= x_{v1} - \frac{D}{2} + \sigma - c_1 y_{v1} - c_2 z_{v1},
\end{aligned}$$

where  $x_{vi}$ ,  $y_{vi}$ , and  $z_{vi}$  ( $i = 1, 2$ , and  $3$ ) are the  $x$ ,  $y$ , and  $z$  coordinates of the vertices of an interacting facet of P2, with  $v_1$  representing the vertex closest to the P1 face and  $v_2$  and  $v_3$  the adjacent vertices (see Fig. 1g). This equation is derived in *Supporting Information*.

While this simple linear form of  $d_x$  and the power-law form of  $U_{\text{rod}}$  make Eq. (2) always analytically solvable, two geometrical aspects of the system require the integral to be solved in a piecewise manner. First, the function  $d_x(y, z)$  is different for each interacting face of P2, where there could be up to three such facets depending on particle position and orientation. Second, the  $y$  and  $z$  integration limits for each facet, which are not constants but functions of each other, need to be defined in a way that yields an analytical solution to the integral Eq. (2). Therefore, we segment the area integral into multiple regions  $r$  in which the  $y$  integral limits are constants and the  $z$  integral limits are linear functions of  $y$ . For two interacting cubes, we first define the intersection area of the  $y$ - $z$  projections of P1 and P2 faces as depicted by the shaded regions in Fig. 1g. Then, we divide the intersection area from each face of P2 into separate regions at all  $y$  positions where the  $z$  integral limits change their dependency on  $y$ , for example, at vertex positions where the edges change their slope (Fig. 1h). This choice makes Eq. (2) analytically solvable and the region definition process can be automated into a computational routine. The final form of the vdW energy integral for each region  $r$  and rod interaction component  $\nu$  is then given by

$$U_{\text{vdW}}^{\nu,r} = \gamma C_\nu \int_{y_{r,1}}^{y_{r,2}} \int_{z_{r,1}(y)}^{z_{r,2}(y)} \left( \frac{\sigma}{d_{r,x}(y, z)} \right)^{n_\nu} dz dy, \quad (5)$$

where  $y_{r,1}$ ,  $y_{r,2}$ ,  $z_{r,1}(y) = b_{r,1}y + a_{r,1}$ , and  $z_{r,2}(y) = b_{r,2}y + a_{r,2}$  represent the integral limits of a region  $r$ , and the total vdW interaction energy between the two NPs is given by  $U_{\text{vdW}} =$

Table 1: Analytical solution of  $U_{\text{vdW}}^{\nu,r}$  for all four types of facet orientations.

Orientation	Solution*
$d_{r,x} \equiv d_{r,x}(y, z)$	$\frac{\gamma C_\nu \sigma^{n_\nu}}{c_{r,2}(n_\nu-1)(n_\nu-2)} \sum_{i=1}^2 \sum_{j=1}^2 \frac{(-1)^{i+j} [a_{r,j}c_{r,2}+c_{r,3}+(c_{r,1}+b_{r,j}c_{r,2})y_{r,i}]^{2-n_\nu}}{(c_{r,1}+b_{r,j}c_{r,2})}$
$d_{r,x} \equiv d_{r,x}(y)$	$\frac{\gamma C_\nu \sigma^{n_\nu}}{c_{r,1}^2(n_\nu-1)(n_\nu-2)} \sum_{i=1}^2 \frac{(-1)^i [c_{r,1}(a_{r,1}-a_{r,2})(n_\nu-2)+(b_{r,1}-b_{r,2})(c_{r,3}+c_{r,1}y_{r,i}(n_\nu-1))]}{(c_{r,1}y_{r,i}+c_{r,3})^{n_\nu-1}}$
$d_{r,x} \equiv d_{r,x}(z)$	$\frac{\gamma C_\nu \sigma^{n_\nu}}{c_{r,2}^2(n_\nu-1)} \sum_{i=1}^2 \sum_{j=1}^2 \frac{(-1)^{i+j} [a_{r,j}c_{r,2}+c_{r,3}+b_{r,j}c_{r,2}y_{r,i}]^{n_\nu-2}}{b_{r,j}(2-n_\nu)}$
constant $d_{r,x}$	$\frac{\gamma C_\nu \sigma^{n_\nu}}{c_{r,3}^{n_\nu}} (y_{r,1} - y_{r,2}) [(y_{r,1} + y_{r,2})(b_{r,1} - b_{r,2}) + 2(a_{r,1} + a_{r,2})]$

\*Analytical solutions for special cases in which the denominators of these expressions are zero whereupon the expressions become undefined are provided in *Supporting Information*.

$\sum_\nu \sum_r U_{\text{vdW}}^{\nu,r}$ . The analytical solution to this integral depends on the particle orientations as  $d_{r,x}$  of a region may or may not be a function of both  $y$  and  $z$ . For example, parallel facets lead to a constant  $d_{r,x}$  while their rotation about axes parallel to the  $y$ - and  $z$ -axis leads to  $d_{r,x} \equiv d_{r,x}(z)$  and  $d_{r,x} \equiv d_{r,x}(y)$ , respectively. Table 1 provides the analytical solutions to the general case in which  $d_{r,x}$  is a function of both  $y$  and  $z$  and to these three special cases. We refer readers to *Supporting Information* for complete derivation of these solutions.

The last remaining task involves establishing suitable values of the unknown parameters  $C_\nu$  and  $n_\nu$  that describe the strength and distance scaling of the attractive and repulsive portions of the rod potential  $U_{\text{rod}}$  (Eq. 3). To obtain these parameters, we attempted power-law fits to the distance  $d_x$ -dependent vdW interaction energies computed between a rod and a NP (of similar dimension  $D$ ) using atomistic descriptions of the two bodies. In particular, the NP was modeled as a simple-cubic lattice of atoms of size and lattice spacing  $\sigma$ , the rod was modeled as a linear array of atoms of same size and spacing, and the interaction energy  $U_{\text{rod}}$  was obtained by summing the interatomic LJ potential with parameters  $\sigma$  and  $\varepsilon$  across all atoms of the rod and NP. For fitting purposes, we decomposed  $U_{\text{rod}}$  into attractive and repulsive contributions  $U_{\text{att}}$  and  $U_{\text{rep}}$  arising from the two terms in the LJ potential.

Figure 1i presents  $U_{\text{rod}}(d_x)$ ,  $U_{\text{att}}(d_x)$ , and  $U_{\text{rep}}(d_x)$  plots computed for a representative

Table 2: Power law coefficients and exponents of the rod potential.

Shape	$D(\sigma)$	$C_{\text{att1}}(\varepsilon)$	$n_{\text{att1}}$	$C_{\text{att2}}(\varepsilon)$	$n_{\text{att2}}$	$C_{\text{rep}}(\varepsilon)$	$n_{\text{rep}}$
Cube	25	-7.76	3.45	-5.87	3.00	3.86	10.66
Cube	50	-7.76	3.43	-4.65	2.72	3.86	10.66
Cube	75	-7.76	3.43	-4.03	2.58	3.86	10.66
Cube	100	-7.76	3.43	-3.65	2.50	3.86	10.66
Triangular prism	50	-7.76	3.44	-4.69	2.73	3.86	10.66
Square rod	50	-7.75	3.44	-4.61	2.71	3.86	10.66
Square pyramid	50	-7.76	3.44	-4.72	2.74	3.86	10.67

nanocube of edge length  $D = 50\sigma$  (which corresponds to a particle of size  $\sim 17$  nm if it were made of metal atoms typically of size  $3.4 \text{ \AA}$ ) along with power-law fits to the attractive and repulsive energies. The energies and fits for other cube sizes ( $D = 25\sigma$ ,  $75\sigma$ , and  $100\sigma$ ) are provided in Fig. S2. The repulsive vdW interactions for all four systems could be fitted by a single power-law (Table 2). The attractive vdW energies, however, could not be fitted using a single power-law, but separating the interactions into a short-range portion  $U_{\text{att1}}(d_x \leq d_{\text{cut}})$  and a long-range portion  $U_{\text{att2}}(d_x > d_{\text{cut}})$  using  $d_{\text{cut}} = 2\sigma$  allowed accurate fits using two separate power laws for all studied NPs. The obtained fit parameters, as listed in Table 2, show that the short-range portions exhibit nearly identical scalings for all nanocubes, but the long-range portions displayed some dependence on particle size. These results suggest that the rod potential needs to be treated as a piecewise continuous function:

$$U_{\text{rod}}(d_x) = \begin{cases} U_{\text{att1}}(d_x) + U_{\text{rep}}(d_x) - U_{\text{att1}}(d_{\text{cut}}) - U_{\text{rep}}(d_{\text{cut}}) + U_{\text{att2}}(d_{\text{cut}}), & d_x \leq d_{\text{cut}} \\ U_{\text{att2}}(d_x), & d_x > d_{\text{cut}}, \end{cases} \quad (6)$$

where  $-U_{\text{att1}}(d_{\text{cut}}) - U_{\text{rep}}(d_{\text{cut}}) + U_{\text{att2}}(d_{\text{cut}})$  was added for  $d_x \leq d_{\text{cut}}$  to make the energies continuous. We set  $U_{\text{rep}} = 0$  for  $d_x > d_{\text{cut}}$ , as the repulsive portion decays to negligible values ( $\ll \varepsilon$ ) before reaching the cutoff distance  $d_{\text{cut}}$ . The results also suggest that the rod potential needs to be re-parameterized for each NP size. We also found that the parameters remain roughly similar for other particle shapes (triangular prisms, square rods, and square pyramids) as long as their overall sizes are comparable (Table 2).

**Model Predictions and Accuracy.** To evaluate the accuracy of our analytical model, we compared its energy predictions for a range of NP shapes and sizes to energies computed atomistically *via* summation of interatomic LJ interactions. For a two-particle system, the energy landscape can be conveniently described in terms of the position and orientation of one NP (P2) relative to the other (P1) in a coordinate frame in which one of P1’s faces ( $\mathcal{F}_1$ ) points in the  $+x$  direction (as in Fig. 1b). The orientation of P2 was described using 3 Euler angles  $(\phi, \theta, \psi)$  and its position was described using 3 Cartesian coordinates  $(d_s, d_y, d_z)$ . We chose to define P2’s position not by its center of mass but by its vertex closest to  $\mathcal{F}_1$ , with  $d_s$  denoting the distance of this vertex from  $\mathcal{F}_1$  and  $d_y$  and  $d_z$  representing the vertex’s lateral offset from the edges of  $\mathcal{F}_1$ . Hence,  $d_s$  represents the closest separation distance between the two NPs, wherein  $d_s = 0$  signifies contact. Using this set of coordinates, we sought to assess the ability of our model to capture the entire vdW energy landscape, especially its distance dependence  $U_{\text{vdW}}(d_s)$  for arbitrary NP configurations  $(d_y, d_z, \phi, \theta, \psi)$ .

*50 $\sigma$  nanocubes.* We first examined  $U_{\text{vdW}}(d_s)$  for parallel configurations ( $\phi = \theta = \psi = 0^\circ$ ) of  $D = 50\sigma$  nanocubes exhibiting different lateral offsets  $d_y$  and  $d_z$ . The results plotted in Fig. 2a show that the model accurately captures the vdW energy profiles computed from atomistic summation. Importantly, the model is able to replicate the location and depth of the energy minimum, the sharpness of the repulsion at short distances, and the long-ranged nature of the attraction. To further assess the model’s accuracy, we calculated the energies for an ensemble of configurations spanning the entire range of  $d_y$  and  $d_z$  values at two distances  $d_s = 1\sigma$  and  $5\sigma$  representative of short- and long-ranged interactions. The obtained  $U_{\text{vdW}}(d_y, d_z)$  landscapes also revealed excellent agreement between model and atomistic summation (Fig. 2b,c). Interestingly, the energies vary almost linearly with the projected overlap area between nanocubes given by  $d_y \times d_z$ . This is more apparent in Fig. 2a where the fully-overlapped configuration ( $d_y = d_z = D$ ) has an energy roughly two and four times larger than those with half ( $d_y = D/2, d_z = D$ ) and one-fourth ( $d_y = d_z = D/2$ ) of their surfaces overlapping. Since our analytical model involves an area integral over the

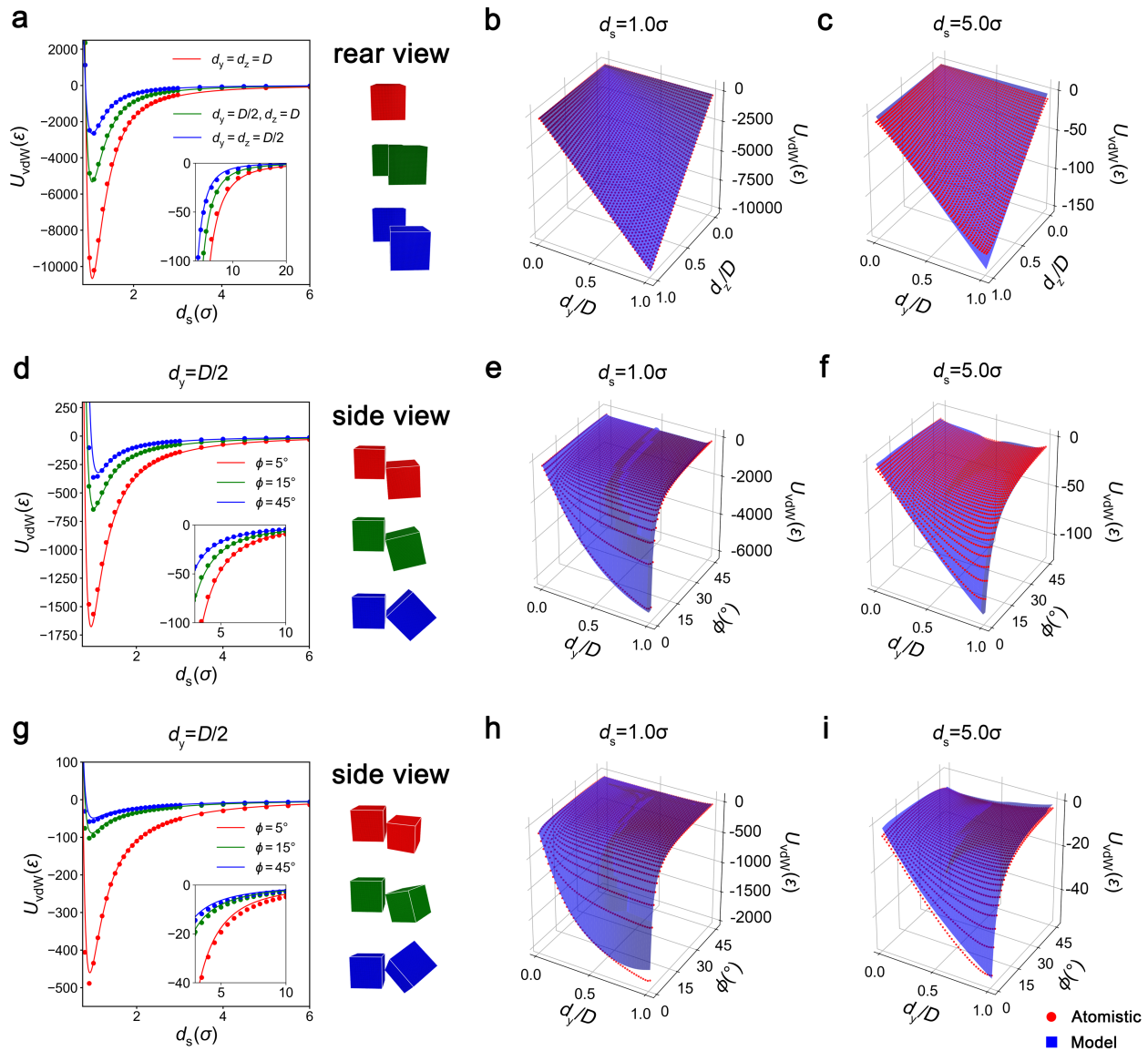


Figure 2: Comparison of vdW energies calculated from the model (solid lines or surfaces) and atomistic summation (symbols) for  $D = 50\sigma$  nanocubes. The plots correspond to results for: (a–c) parallel, (d–f) tilted coplanar, and (g–i) general configurations. Insets show long-ranged energies.

interacting regions, the model describes this linear dependence accurately.

Next, we examined tilted coplanar configurations, where nanocubes lie flat on a plane and translate and rotate only within that plane, configurations relevant to particles confined in thin films or those deposited on flat substrates.<sup>10,28</sup> Such configurations are characterized by the separation distance  $d_s$  between nanocubes, their lateral offset  $d_y$ , and their tilt angle

$\phi$ , assuming that particles lie flat on the  $x$ - $y$  plane ( $\theta = \psi = 0^\circ, d_z = D$ ). Figure 2d-f presents model predictions for  $U_{\text{vdW}}(d_s)$  at representative  $d_y$  and  $\phi$  values and for  $U_{\text{vdW}}(d_y, \phi)$  at the two representative  $d_s$  values considered above. We find that the model is able to quantitatively capture the distance dependence of the vdW energy and its dependence on the relative offset and tilt for these nanocube configurations. The  $U_{\text{vdW}}(d_y, \phi)$  landscapes also reveal that the vdW energy rises with increasing  $d_y$ , as expected, but unlike the linear dependence observed for parallel configurations, the energies for tilted cubes display increasingly weaker dependence on  $d_y$  with increasing  $\phi$ . The reason is that the larger the  $\phi$ , the more the total energy is dominated by the interactions mediated by the leading edge of P2 (closest to P1) which are unaffected by changes in  $\phi$  at fixed  $d_s$ . The landscapes also show the energy decreasing more sharply with increasing  $\phi$  at smaller  $\phi$  than larger  $\phi$ . This effect may be explained by considering the incremental change in vdW interactions mediated by a rod element on P2 (any rod not associated with the closest vertex) that moves away from P1 by a small distance due to a small increase in angle  $\phi$ . Because  $U_{\text{rod}}(d_x)$  decays more sharply at smaller distances, rods that are located closer to P1 at small  $\phi$  will incur a sharper drop in vdW interactions compared to those further away at large  $\phi$ . Both of these effects are accurately captured by the analytical model.

Lastly, we tested our model for the more general case wherein nanocubes are able to rotate or translate along all six degrees of freedom. Given the enormity of this configurational space, we chose to focus on configurations with  $\phi = \theta = \psi$  and  $d_z = 0.5D$  as we found these to be general enough to capture the model's accuracy for any configuration.  $U_{\text{vdW}}(d_s)$  plotted for several representative orientations in Fig. 2g shows that the model can accurately describe the depth of the energy minimum and the long-range interactions. However, the location of the repulsive barrier at small distances is slightly overpredicted at large  $\phi$ . This is because the model treats NPs as macroscopic bodies with flat surfaces while the actual particles have atomically corrugated surfaces that may allow closer separation distances, as P2's leading vertex could be accommodated within the atomic interstices of P1's interacting

face. This discrepancy in barrier location is however smaller than  $0.1\sigma$ , so quite negligible. The model also reproduces well the atomistically computed  $U_{\text{vdW}}(d_y, \phi)$  landscapes at small and large separation distances (Fig. 2h,i). Similar to coplanar configurations, the energies for these general configurations also vary highly nonlinearly with the relative offset and tilt of the nanocubes, and the model is again able to quantitatively capture all these variations spanning at least three orders of magnitude in energy.

*Error analysis.* To more thoroughly analyze the model’s accuracy for the above nanocubes, we evaluated the prediction error for a wide range of parallel, tilted coplanar, and general configurations, as shown in Fig. 3. Each data point in the figure corresponds to the collective error  $\sum |U_{\text{model}} - U_{\text{atomistic}}| / \sum |U_{\text{atomistic}}|$  in the predicted energies of all configurations with that specified coordinate value, where  $U_{\text{model}}$  and  $U_{\text{atomistic}}$  are the energies calculated by the model and by atomistic summation. For example, the data point marked with a blue square in Fig. 3g represents the collective error in the energy of all general configurations ( $0 < d_y \leq D$  and  $0^\circ < \phi \leq 45^\circ$ ) with  $d_s = 11\sigma$ . We have computed these errors with respect to  $d_s$ ,  $d_y$ , and  $d_z$  for parallel configurations, and  $d_s$ ,  $d_y$ , and  $\phi$  with fixed  $d_z$  of  $D$  and  $0.5D$  for the coplanar and the general configurations, respectively. To exclude configurations with negligible interactions, we only considered those with  $U_{\text{atomistic}} > 3\varepsilon$ . By analyzing the error associated with each coordinate in this manner, we were able to examine the strengths and weaknesses of the model for particular types of configurations.

Our results demonstrate that the model is accurate for most configurations and the errors are generally less than 15%. The largest errors are observed for parallel configuration of nanocubes interacting with their edges ( $d_y$  or  $d_z \approx 0$ ) or interacting at large separation distances ( $d_s > 10\sigma$ ), and for strongly tilted configurations of nanocubes interacting *via* vertex-edge contacts ( $\phi > 40^\circ$ ). These larger errors arise due to two factors. First, the magnitude of the energy for these configurations are generally much smaller than for the nanocubes interacting with small  $d_s$ , small  $\phi$ , or large  $d_y$  or  $d_z$ . For instance, the average energy of parallel configurations at  $d_s = 1.5\sigma$  is equal to  $1140\varepsilon$  while those at  $d_s = 10\sigma$  exhibit

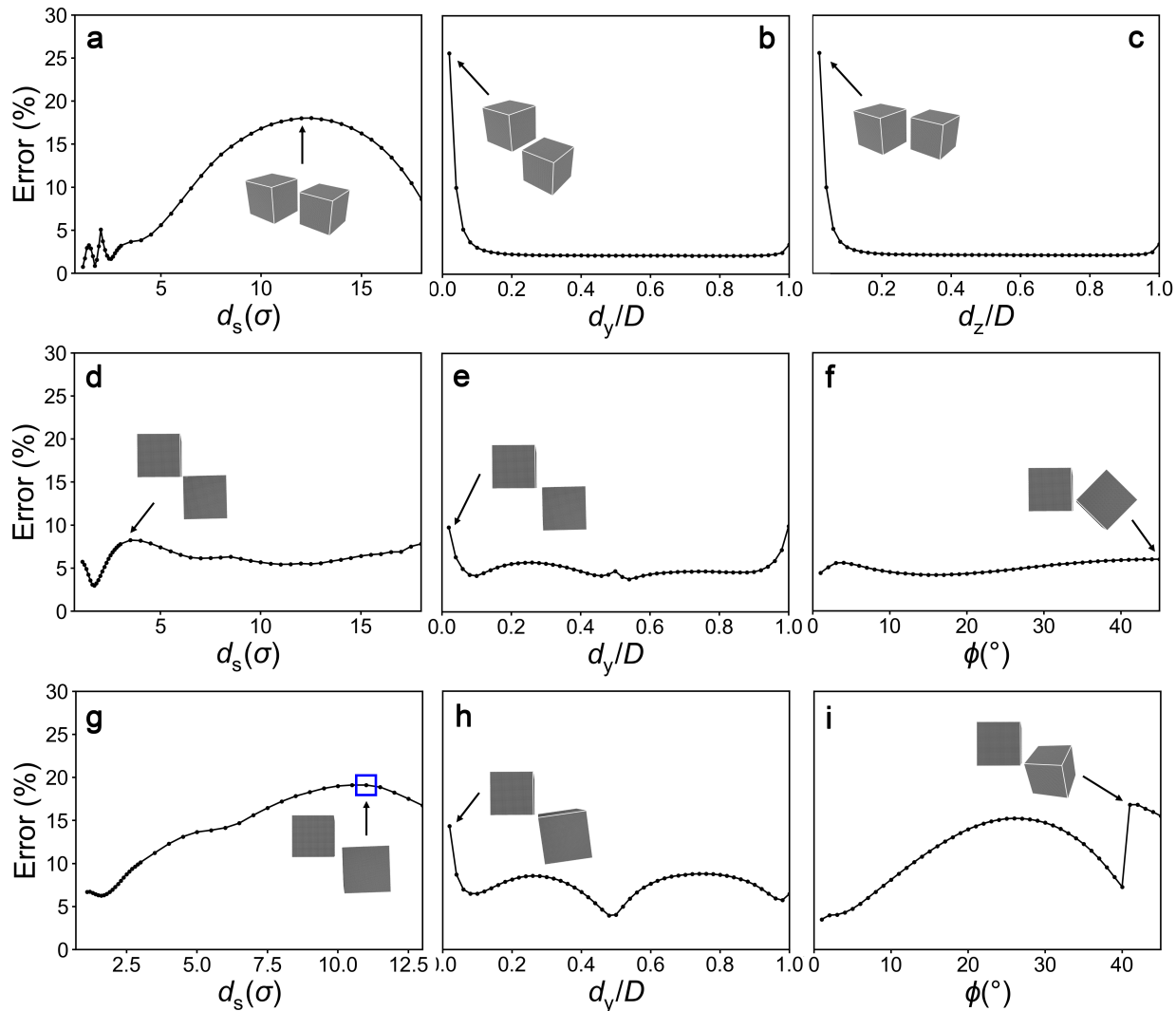


Figure 3: Collective errors of all configurations with the specified coordinate value for (a–c) parallel, (d–f) coplanar, and (g–i) general configurations. Depicted NPs in each plot indicate the configuration with the largest individual errors among all configurations sharing the specified coordinate value. See main text for discussion on the blue box in (g).

an energy of only  $9\epsilon$ . Therefore, even small differences between  $U_{\text{model}}$  and  $U_{\text{atomistic}}$  will result in large percentage errors for configurations with large  $d_s$ . Second, several assumptions of our model become less valid for these configurations. For instance, we assumed that all rods making up particle P2, even those facing P1's edges, interact with particle P1 as if they were facing its center. For the configurations with  $d_y$  or  $d_z \approx 0$ , the interaction energies between the particles are dominated by the energies of the edges and our assumption could lead to errors in such cases.

Although these results point out certain weaknesses of the analytical model due to its assumptions, it is noteworthy that all of the configurations with large individual errors are those in which the particles are interacting very weakly. In fact, almost all configurations of nanocubes with the largest individual percentage errors had  $|U_{\text{atomistic}}| < 4\epsilon$ . Therefore, we can conclude that while our model may deviate from atomistic energy calculations for some weakly interacting configurations, the model is accurate for most configurations and especially for those with significant interaction strengths.

*Other particle sizes and shapes.* To demonstrate that the model is applicable to a wide range of particle sizes, we evaluated the model’s accuracy for three additional sizes of nanocubes:  $D = 25\sigma$ ,  $75\sigma$ , and  $100\sigma$ . We used the power-law parameters listed in Table 2 to make energy predictions for these new systems. Our results for the face-face configuration ( $d_y = d_z = D, \phi = \theta = \psi = 0^\circ$ ) are presented in Fig. 4a; the results for other configurations are provided in Fig. S3. We observe that the analytical model accurately predicts both short and long-ranged interaction energies for all three nanocubes, with the energies scaling roughly proportional to the interaction area for parallel configurations. As the sizes of these nanocubes range from  $\sim 9$  nm to  $\sim 34$  nm in physical units (if one assumed metallic NPs with  $\sigma \sim 3.4$  Å), these results demonstrate that the model is directly applicable to experimentally relevant NP sizes.<sup>46–48</sup>

We finally investigated the ability of our model to describe the vdW interactions between other types of faceted NPs. For this purpose, we examined triangular prisms (of dimensions  $50\sigma \times 50\sigma \times 70.7\sigma$ ), square rods ( $50\sigma \times 50\sigma \times 500\sigma$ ), and square pyramids ( $50\sigma \times 50\sigma \times 50\sigma$ ), as shown in Fig. 4b. These particular NP shapes were chosen as they have been extensively explored in the literature for studying packing behavior and self-assembly,<sup>49–51</sup> and for creating devices with unique plasmonic<sup>52,53</sup> and chiroptical properties.<sup>54,55</sup> We restricted our analysis to particle configurations most relevant to their application, namely, tilted coplanar configurations for triangular prisms (that yield distance- and angle-dependent plasmonic hotspots), twisted configurations for square rods (used for chiroptical sensing), and face-tip configura-

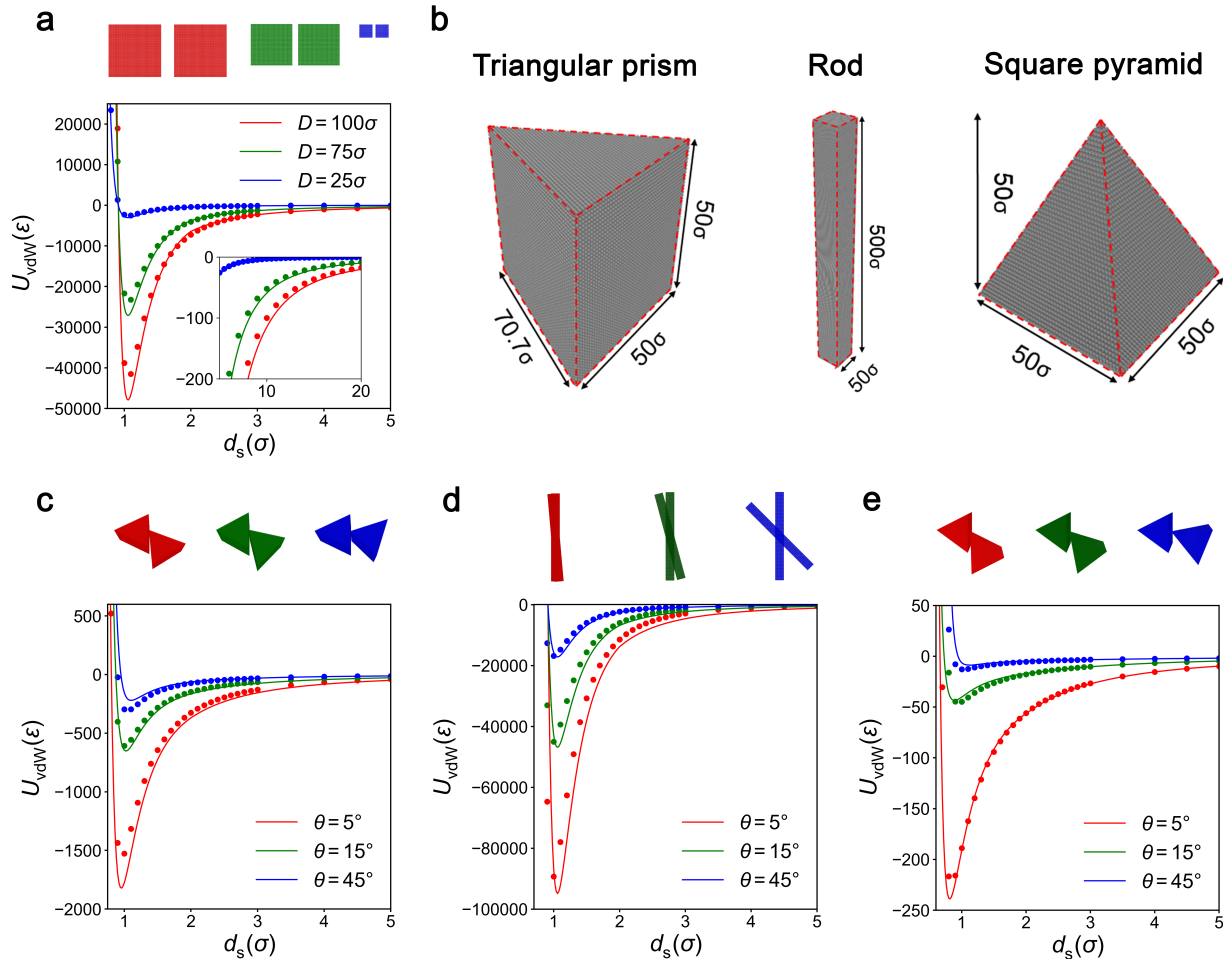


Figure 4: Comparison of vdW energies obtained from the model (solid lines) and atomistic summation (symbols) for different-sized nanocubes and other NP shapes. (a) Energies of nanocubes of varying sizes in face-face configuration. Inset shows long-ranged energies. (b) Schematics of the three additional NP shapes studied. Energies of (c) triangular prisms in coplanar configuration at varying slant angle, (d) parallel rods at varying dihedral angles, and (e) square pyramids in tip-face configurations at varying orientations.

tions for square pyramids (commonly observed during assembly and packing). Figure 4c-e presents representative  $U_{\text{vdW}}(d_s)$  for the three NP shapes in various configurations calculated using the parameters listed in Table 2. We observe that for all three NPs our model accurately reproduces the distance and orientation dependence of the vdW energies obtained from atomistic summation. The model's accuracy is especially reassuring for triangular prism and square pyramid configurations exhibiting small tilt angles  $\theta$  that most strongly challenge the fixed rod-length approximation in our model. For these configurations, rod elements at the

leading edge (in case of triangular prisms) or leading vertex (square pyramids) of P2 are actually only a single atom long. This indicates that our rod-length approximation may not be as erroneous as it appears at first glance. For parallel rods, the variation in vdW energy with twist angle was found to match the variation in surface area of interaction with angle, which also our model predicted very well. Taken together, our results demonstrate that our analytical model is applicable to faceted NPs of various shapes and sizes.

**Analysis of Model Assumptions.** In deriving our analytical model for vdW interaction energies between faceted NPs, we made the following four assumptions: (1) all rod elements irrespective of their lateral position are of length equal to the characteristic size of the NP (*rod length approximation*); (2) each rod element irrespective of its lateral position contributes an interaction energy equal to that of a rod facing the center of reference particle P1 (*edge approximation*); (3) energies from all rod elements that are not within the boundary of the interacting face of P1 in the  $y$ - $z$  axes are ignored (*cutoff assumption*); and the rod-NP interaction potential  $U_{\text{rod}}$  can be described by power-law functions of fixed coefficients and exponents (*power-law approximation*). Despite these assumptions, we found that the analytical model provides remarkably accurate predictions for the vdW interaction energy between nanocubes in almost every possible configuration. The model also makes accurate predictions for other faceted particles like rods, prisms and pyramids in relevant configurations. Thus, several of the model assumptions, which appear to become worse with tilted configurations of nanocubes and glancing tip-face configurations of prisms and pyramids, do *not* lead to significant errors in net energy.

*Rod length, edge, and cutoff assumptions.* To understand in depth how these assumptions affect the accuracy of energy predictions, we first examined their validity at the level of *rod-NP interactions* by evaluating the LJ energies contributed by individual atoms of a  $D = 15\sigma$  nanocube and a rod of same length facing the nanocube's center at varying distances  $d_x$ . We chose a small NP for analysis, as it allowed better visualization of atomic energies. The results of our analysis are shown in Fig. 5a, where we have colored each atom according

to their energy contribution. We find that the validity of the rod length, edge, and cutoff assumptions all depend on  $d_x$ . For  $d_x = 0.7\sigma$ , where the end atom of the rod overlaps with one of the nanocube atoms, the rod-NP energy is described almost entirely by the interaction energy of the two overlapping atoms. Therefore, for rods that overlap with the particle ( $d_x \lesssim 1\sigma$ ), the fixed rod length assumption induces negligible errors, as the contribution from the non-overlapping atoms that we fictitiously add or remove to keep the rod length fixed should be negligible compared to the contributions from the closest set of atoms. Since the rod-NP energy depends completely on the overlapping nanocube atom that has the same lateral position as the rod, the error resulting from the edge assumption should also be negligible, as the interaction energy of a rod facing the center of a nanocube should be equivalent to that of a rod at or near the edge. The cutoff assumption is also valid as only those rods within the  $y$ - $z$  boundaries of the nanocube will be able to overlap with it.

As  $d_x$  becomes larger, the number of atoms contributing significant interaction energies increases. The data in Fig. 5a indicates that these atoms can be enclosed by a sphere centered around the rod atom closest to the nanocube. As this sphere gets larger with increasing  $d_x$ , the assumptions become worse. For example, at  $d_x = 1.5\sigma$  and  $3\sigma$ , the energies contributed by nanocube atoms in the immediate vicinity of the central atom facing the rod also become significant. In this case, if the rod was facing the edges of the nanocube, our model would overestimate the rod's energy by an amount equal to the energy contributed by some of these vicinity atoms that the model assumes to exist. However, we find that the energy is still dominated by the energy of the single atom closest to the cube, and, therefore, the rod length, edge, and cutoff assumptions still remain quite valid. When  $d_x$  increases further to  $10\sigma$ , almost the entire interacting face of the nanocube makes significant contribution to the energy of the system. Thus, if distant rods facing the edges of the nanocube are made to interact at the nanocube center based on the edge approximation, we would overestimate the total energy by adding contributions from many nanocube atoms that do not actually exist. Furthermore, the rod atoms make significant energy contributions up to the fourth

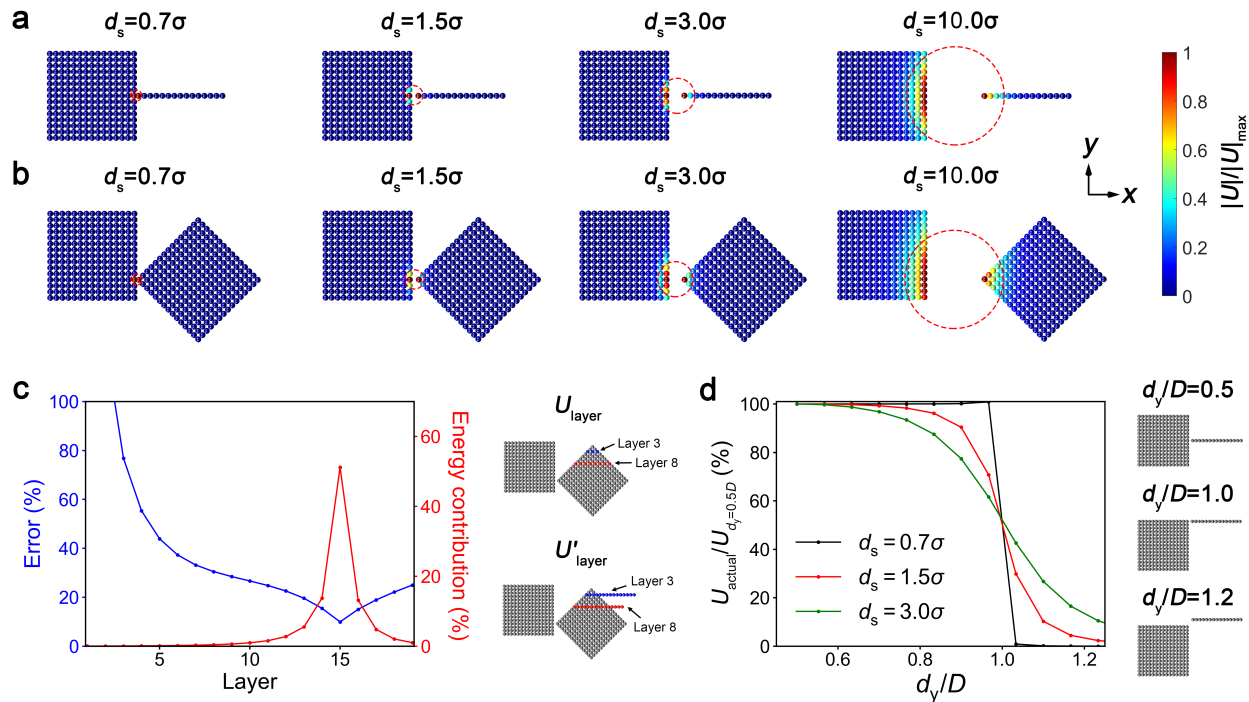


Figure 5: Analysis of model's rod length, edge, and cutoff assumptions for  $15\sigma$  nanocubes. (a,b) vdW energies contributed by individual atoms to the overall interaction energy of: an atomistic rod facing the center of mass of an atomistic cube (a), and two coplanar atomistic cubes with  $d_y = 0.267D$ ,  $d_z = D$ ,  $\phi = 45^\circ$ , and  $\theta = \psi = 0^\circ$  (b). In both cases, the  $z = 0$  cross-section is shown and the coloring scheme is based on the magnitude of each atom's energy compared to that exhibiting the largest energy in each particle. Red dashed circles highlight atoms with significant energy contributions. (c) Energy contribution by each layer of atoms along the  $y$  direction plotted as percentage of total energy (red), and percentage error in the energy of each layer calculated by assuming they are made of rods of fixed length  $D$  (blue). (d) vdW interaction energy of atomistic rods as a function of their position along the  $y$ -axis for rods held at three distinct separation distances.

layer. Therefore, for highly slanted cubes or triangular prisms that are one-atom thick in the  $x$ -axis at the tips, the rod-length assumption would lead to excess energy from the fictitious layers of added rod atoms. Finally, as the volume of sphere of influential atoms increases, the cutoff assumption also becomes worse, as rods above or below the nanocubes top or bottom edges, currently neglected in our model, start to make more significant contributions.

To assess the impact of the rod-length, edge, and cutoff assumptions at the level of *inter-particle interactions*, we analyzed the interatomic LJ interactions between two  $15\sigma$  nanocubes in a tilted coplanar configuration at varying separation distances  $d_s$ , as depicted in Fig. 5b.

We chose this configuration in which NPs interact mostly *via* their edges, as it invokes some of the largest errors from these assumptions. As observed in the rod-cube system, the number of atoms contributing significant energies expanded with increasing  $d_s$ . For example, while the total energy of the system could be almost entirely described by the interaction energy of the overlapping atoms at  $d_s = 0.7\sigma$ , the total energy for  $d_s = 10\sigma$  required consideration of a larger number of atoms from both NPs. This means that our rod-cube model for this well-separated configuration would treat particle P1 as if it had many more atoms that fill up the red dotted circle drawn in the figure. However, it is important to note that the majority of the total energy is still contributed by atoms around the closest vertex of P2 and P1 atoms facing this vertex. Though the model is expected to yield large errors for rods corresponding to the upper and lower edges of P2 which are actually only one atom long in the  $x$ -axis and have large  $d_x$ , the contribution of these atoms to the overall energy is negligible. Since the model calculates the contribution from the atoms around the closest vertex accurately, the net error in vdW energy, even for this highly slanted nanocube P2 interacting near the edge of P1, remains small.

To gain a more quantitative understanding of the error introduced by the rod length assumption, we compared in Fig. 5c the energies contributed by each layer of atoms in P2, from top to bottom. In the figure, layer 1 corresponds to the single atom on the top edge of the cube, layer 2 represents the next layer of atoms immediately below that edge, and so on, with layer 15 signifying the layer of atoms containing the P1-proximal vertex. The blue curve represents the percentage error  $|(U'_{\text{layer}} - U_{\text{layer}})/U_{\text{layer}}|$  in the energy of each layer measured as the deviation of its energy  $U'_{\text{layer}}$  calculated using full-length rods of atoms (of length  $D$  as assumed in our model) from the true energy  $U_{\text{layer}}$  calculated using the actual atomic positions in each layer, and the red curve represents the percentage energy contribution of each layer as given by  $U_{\text{layer}}/\sum U_{\text{layer}}$ . The results show that the error is indeed very large for the topmost layers ( $> 100\%$  for layer 1) and dips to small values for layers involving or adjacent to the closest vertex ( $\approx 10\%$  for layer 15). However, the energies contributed

by the topmost layers are only a tiny fraction of the total energy (0.016% for layer 1), as most of the energy is contributed by layer 15 ( $\approx 51\%$ ) and its adjacent layers. This explains why the cumulative error in total energy remains quite small, at only 14.4%, even though the percentage errors in energy are quite large for layers close to the edges of the nanocube. These results demonstrate that the rod length assumption has a small negative impact on the total energy of particles, as the portions of P2 that most violate this assumption are almost always the farthest from P1 (e.g., at the tips of particles in highly slanted configurations where the rod lengths deviate the most from the assumed length  $D$ ) and hence contribute the least to the total energy.

To quantify the errors arising from the edge and cutoff assumptions, we examined how the rod-nanocube interaction energy varies as a function of the rod's lateral position. Figure 5d plots the LJ interaction energy between the  $15\sigma$  nanocube and a same-length rod as a function of its normalized lateral coordinate  $d_y/D$ , where  $d_y/D = 0.5$  and  $1$  correspond to a rod facing the nanocube's center and upper edge, and  $d_y/D > 1$  indicates a rod going beyond the upper edge; we held the other lateral coordinate fixed at  $d_z = D/2$  and compared the energy variation at three different fixed values of the separation distance  $d_x$ . For a rod with  $d_x = 0.7\sigma$  that overlaps with the nanocube, the energy remains unchanged from the center to the edge of the nanocube and becomes negligible immediately after the rod crosses the edge. The edge and cutoff assumptions are thus valid for small separation distances, and should lead to negligible errors for NP configurations at small separation distances. At larger  $d_x$ , the energies start to deviate as  $d_y/D$  exceeds 0.8 and becomes  $\approx 70\%$  of the energy of the centrally-located rod once the rod gets to the edge of the nanocube. Beyond the edge, the energy quickly reduces to  $\approx 15\%$  of the energy of the central rods. This means that the edge assumption may overestimate the vdW energy of a rod at the edge by 30%, and the cutoff assumption may underestimate its energy slightly below the edges by 15%. The net impact of the two kinds of errors on interparticle energy will obviously be much smaller because the errors partly cancel out due to their opposite sign, they diminish with rod distance from

edges, and the percentage contribution of energy from rods close to edges to the net energy is typically small. Thus, similar to the rod length assumption, the edge and cutoff assumptions also lead to small errors in the total energy.

*Power-law approximation.* Another source of error stems from our assumption that the rod potential  $U_{\text{rod}}(d_x)$  can be approximated by simple power-law functions with constant parameters (Table 2). For instance, the repulsive portion  $U_{\text{rep}}$  of this potential for  $50\sigma$  nanocubes was described using a single power law with scaling exponent  $n_{\text{rep}} = 10.66$  and its attractive portion  $U_{\text{att}}$  was described using two power law with exponents  $n_{\text{att}} = 3.43$  when  $d_x \leq 2\sigma$  and  $n_{\text{att}} = 2.72$  when  $d_x > 2\sigma$ . However, explicit determination of distance scalings from an atomistically-computed rod potential for this nanocube revealed that both  $n_{\text{rep}}$  and  $n_{\text{att}}$  are continuously varying functions of  $d_x$  (Fig. 6a). This is expected as the distance-scaling of the interaction between macroscopic bodies depends on the comparative length scales of the particles and their separation distances. In fact, in the limit  $d_x \gg D$ , the internal differences in the positions of atoms within the rod and the NP become miniscule compared to  $d_x$ , and  $n_{\text{rep}}$  and  $n_{\text{att}}$  should approach values of 12 and 6, the distance scalings of interatomic LJ interactions.

The above analysis shows that *distance-dependent* scaling exponents might be required to accurately model  $U_{\text{rep}}$  and  $U_{\text{att}}$  across all  $d_x$ , though this would make the model analytically intractable. Thus, our strategy of modeling these potentials using one or two power-laws with *constant* exponents to permit analytical solution is approximate. Given that  $U_{\text{rep}}$  needs to be modeled accurately only over small distances ( $d_x \leq 2\sigma$ ) due to the short-ranged nature of this potential and that its true exponent shows only a small variation in this distance range, the power-law approximation turns out to be very accurate for  $U_{\text{rep}}$  (see Fig. 1i). The power-law used for modeling  $U_{\text{att}}$  at short distances is similarly a good approximation as this power-law also is required to operate over a short range of distances ( $1\sigma \leq d_x < 2\sigma$ ). However, the power-law used for modeling the long-range behavior of  $U_{\text{att}}$  needs to be accurate over broader range of distances ( $d_x > 2\sigma$ ). Clearly, this power-law is neither expected nor required to

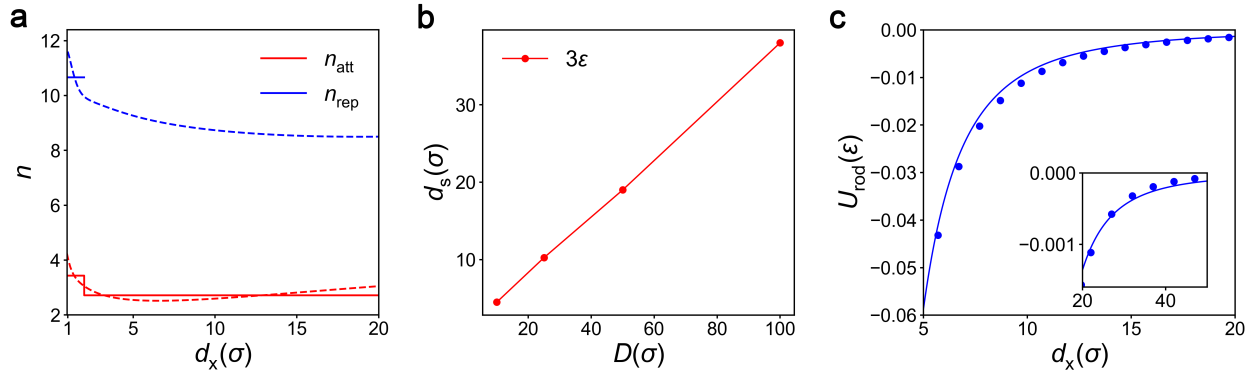


Figure 6: Analysis of model's power-law approximation for  $50\sigma$  nanocubes. (a) Scaling exponents  $n_{\text{att}}$  and  $n_{\text{rep}}$  of the attractive and repulsive portions of the rod potential as function of distance  $d_x$ . Solid lines represent fitted exponents and their assumed range of validity, while dashed lines represent true exponents obtained from atomistic rod-nanocube interactions. (b) Separation distance  $d_s$  at which the interparticle vdW energies have decayed to  $\leq 3\epsilon$  plotted as a function of particle size  $D$  for nanocubes in face-face configurations. (c) Rod potential calculated atomistically (symbols) and compared against its power-law model over a distance range of  $d_x \leq D$  (solid line).

accurately model interactions at large distances where the fitted exponent departs strongly from the true exponent and the interaction energies become very small. We therefore set the range of validity of this power law as the distance range over which the particles still interact with significant energies that we want our model to accurately predict; in this study, we set this energy threshold to be equal to  $3\epsilon$ , which is  $\mathcal{O}(k_B T)$ .

To determine roughly the distance range for which the total interparticle energy  $|U_{\text{vdW}}| > 3\epsilon$ , we calculated via atomistic summation the interaction energies of face-face nanocubes for a range of cube sizes  $D$ . We chose this configuration, as it yields the largest energies for a given  $d_s$ . Interestingly, the energies decayed to  $3\epsilon$  at  $d_s \approx 0.38D$ , a distance range proportional to particle size (Fig. 6b). For nanocubes with  $\phi > 0^\circ$  or  $d_y < D$ , the relevant  $d_s$  would be even smaller. Therefore, our model is only required to be accurate for  $d_s \leq 0.38D$ . As demonstrated in our results in Fig. 3, our model using only the two sets of power laws described above could accurately predict vdW interaction energies within this distance range. In fact, the single power-law used for describing the long-range portion of  $U_{\text{att}}$  in our model could accurately describe  $U_{\text{rod}}$  at distances as large as  $d_s = 1D$  (Fig. 6c). Therefore, we can

assume that our current model with two sets of parameters can predict the vdW interactions between faceted NPs over a significant range of separation distances. Additional power-laws could potentially be included in the model if greater accuracy is required for predicting small interparticle energies at larger  $d_s$ .

**Computational Implementation.** To make the model more accessible to researchers and demonstrate its applicability, we developed an open-source MATLAB application with a graphical user interface (GUI) that implements the model for arbitrary nanocube sizes and configurations. The user interface is shown in Fig. 7. In this application, the user can input the configuration  $(d_s, d_y, d_z, \phi, \theta, \psi)$  and material properties  $(\sigma, \varepsilon, D)$  of the nanocubes. In addition to utilizing the user-provided values of  $\varepsilon$ , the application can also infer  $\varepsilon$  from the Hamaker constant, atomic diameter, and number density of atoms constituting the material (see *Supporting Information* and Fig. S7 for examples of application of the model to specific materials). From these input parameters, the application calculates and outputs the following: the power-law scaling coefficients and exponents that best describe the short- and long-range portions of the rod potential; the  $y$ - $z$  projection of the interacting regions of the facets used for calculating total energy; and the vdW energies as a function of particle separation distance  $d_s$ , including the value at the inputted distance. The potential energy obtained from the analytical model can also be compared with energy computed from atomistic calculations. Detailed description of the computational implementation of our model is provided in *Supporting Information*, and the application and its source codes are available on GitHub.<sup>56</sup>

## DISCUSSION

In this study, we developed an accurate analytical model for calculating vdW interaction energies between faceted NPs. This work is motivated by the high computational costs of calculating vdW energies through atomistic summation of interatomic potentials and

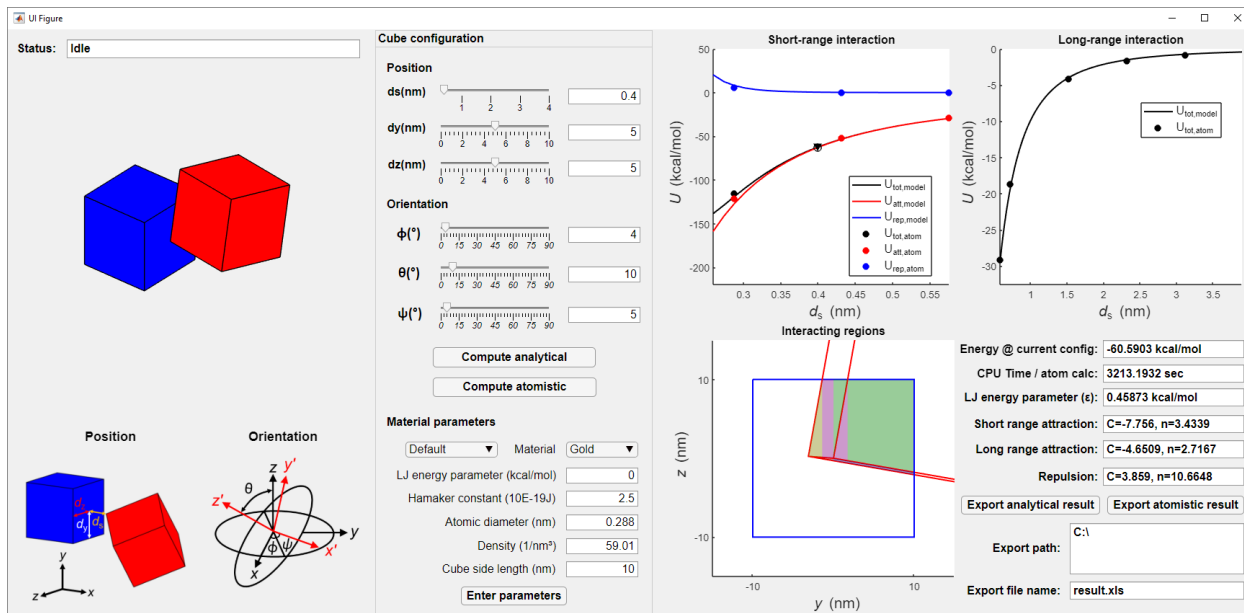


Figure 7: Graphical user interface of the MATLAB application.

the inability of coarser-grained models of particles to capture various features of the vdW energy landscape (comparison between  $U_{\text{vdW}}$  obtained from atomistic models and coarse-grained models is provided in Fig. S5). Our model was derived by discretizing the volume of one of the interacting particles into rod-shaped volume elements and casting the interparticle vdW energy of interaction as an area integral over rod-particle interactions. Through several approximations and atomistic calculations, we were able to derive and parameterize power-law functions for the rod-particle potential. Segmentation of the vdW energy area integral into sub-integrals with constant or linearly-varying integration limits then allowed us to derive closed-form solutions for the vdW energy. We found that the resulting analytical expressions were able to quantitatively capture the distance- and orientation-dependent vdW interactions for a range of faceted NPs, including cubes, square rods, triangular prisms, and square pyramids. Extensive analysis of errors resulting from approximations of the model revealed that the percentage errors in calculated energies were minimal for most particle configurations and that the small fraction of configurations that exhibited larger errors represented weakly interacting particles that have a much lower bar for accuracy.

The obvious benefit of this model over atomistic summation is its computational effi-

ciency. The cost of atomistic energy calculations rises sharply with the particle size, and, for the nanocubes studied here, the CPU time rises as  $\approx 2.6 \times 10^{-7} D^6$  seconds per energy evaluation on an Intel Core i7-7700 processor (Fig. S6). In contrast, our model takes only  $\approx 7 \times 10^{-4}$  seconds of CPU time per evaluation independent of the particle size. For  $100\sigma$  nanocubes, this translates to more than 8 orders of magnitude reduction in computational costs. The model's efficiency would be especially valuable in simulations that require repeated calculation of interparticle energies. Consider, for instance, a Monte Carlo simulation of commonly studied 40 nm ( $\sim 100\sigma$ ) silver nanocubes<sup>47</sup> with a typical system size of  $N = 100$  particles and simulation length of  $10^7$  steps. Assuming  $\mathcal{O}(N)$  energy evaluations per step, the simulation would require  $\sim 200$  hours as opposed to  $\sim 10^6$  years of CPU time if the simulation used our model instead of atomistic summation for calculating energies.

The development of an analytical model for vdW interactions that is both accurate and efficient should enable many problems involving faceted NPs to be studied by simulations that would otherwise have had to resort to inaccurate treatment of vdW interactions *via* coarse-grained models. The vast literature on spherical NPs has shown that the strength and range of attractive forces between particles, including those arising from vdW interactions, significantly impact the rheology, phase behavior, and microstructure of fluid-particle systems. For example, the strength of vdW interactions between particles has been shown to strongly impact their jamming transition<sup>41</sup> and the type of anisotropic phase that they form when grafted with polymers.<sup>57,58</sup> Simulation studies of faceted NPs using purely-repulsive potentials have demonstrated that the particles organize into novel arrangements under compression as a result of the anisotropy in their excluded volume.<sup>33,34</sup> One can expect that the introduction of attractive forces between such NPs would cause them to self-assemble (as opposed to pack) into new and complex equilibrium and nonequilibrium (trapped) structural phases. Thus, the ability to accurately and efficiently model vdW forces between faceted NPs would enable researchers to explore their phase behavior and rheology. Such studies have the potential to reveal previously unseen phases and phenomena that may be of interest

to basic science or engineering applications.

Several extensions of the model that may enhance its applicability but have not been investigated in the current study could become topics of future investigation. First, while we showed that the model provides excellent energy predictions for simple faceted geometries like cuboids, pyramids, and prisms, the range of particle shapes for which the model remains accurate needs to be further investigated. An inherent assumption of our model is that the interactions between two particles is dominated by a single interacting facet of one of the particles (P1's face normal to the  $x$ -axis), which holds true for all shapes whose adjoining facets subtend an angle equal to or smaller than  $90^\circ$ . However, this assumption becomes invalid for shapes exhibiting larger angles, or in other words, shapes with more facets than cubes. For these shapes, other P1 facets also exhibit overlap with P2 facets in their  $y$ - $z$  projections and their interactions must be accounted for as well. Thus, the model is expected to lose accuracy with increasing number of facets (beyond cubes) to the point of becoming invalid for spheres that effectively possess an infinite number of facets. Thus, additional work is required to determine particle shapes for which the model remains accurate and to revise the model to improve its accuracy for other faceted geometries.

Second, we did not investigate in this study the model's accuracy for particles larger than  $D = 100\sigma$  ( $\sim 40$  nm). Based on our earlier analysis of the rod potential, the power-law describing its long-range attraction is required to be valid to a distance of  $0.38D$  (at which point the interparticle interactions are deemed to be insignificant). Thus, the larger the particle, the larger the range over which the power-law is required to be accurate. This means that for large NPs, of sizes 100 nm to several microns, a single power-law may not be sufficient to accurately model the rod potential over this entire range. Future studies would thus benefit from exploring the accuracy of the current version of the model to larger particles and investigating the ability of employing additional power-laws to improve model accuracy for large NPs.

Lastly, the model currently only calculates vdW energies between particles and not forces

or torques, which requires additional and more complex considerations of energy gradients and interaction site positions. Therefore, the model in its current form can only be used in “static” simulations such as Monte Carlo and energy-minimization methods, and not in “dynamic” simulations such as molecular dynamics or Brownian dynamics methods. While static simulations can be used to investigate many particle-related phenomena such as self-assembly and phase behavior, expansion of the model to dynamic simulations would enable other particle-related topics such as assembly dynamics, rheology, and nonequilibrium effects to be studied.

## CONCLUSIONS

We developed an analytical model for calculating the vdW interaction potential between faceted NPs. The model is able to accurately predict the vdW energy landscape across all relevant particle configurations for a range of NP shapes. A computational implementation of this method demonstrated that the model can bring orders of magnitude improvement in computational efficiency over the atomistic summation approach for calculating vdW energies. We expect that the model’s accuracy, efficiency, and ease of implementation will allow researchers to rapidly explore vdW energy landscapes of faceted NPs, and, more importantly, enable many future investigations of faceted NPs through simulations that have so far been impeded by the prohibitive costs of accurately evaluating vdW energies.

## ACKNOWLEDGMENTS

This work was supported by a grant from the National Science Foundation (CMMI award 1636356) and Duke University. Computational resources were provided by the Duke Computing Cluster (DCC) and the Extreme Science and Engineering Discovery Environment (XSEDE) Program supported by the National Science Foundation (ACI-1053575). We thank Dr. Michael Rubinstein and Dr. Stefan Zauscher for useful discussions.

## References

1. Sun, Y.; Xia, Y. Shape-controlled synthesis of gold and silver nanoparticles. *Science* **2002**, *298*, 2176–2179.
2. Pal, J.; Pal, T. Faceted metal and metal oxide nanoparticles: design, fabrication and catalysis. *Nanoscale* **2015**, *7*, 14159–14190.
3. Tian, N.; Zhou, Z.-Y.; Sun, S.-G.; Ding, Y.; Wang, Z. L. Synthesis of tetrahexahedral platinum nanocrystals with high-index facets and high electro-oxidation activity. *Science* **2007**, *316*, 732–735.
4. Huang, X.; Zhao, Z.; Fan, J.; Tan, Y.; Zheng, N. Amine-assisted synthesis of concave polyhedral platinum nanocrystals having {411} high-index facets. *J. Am. Chem. Soc.* **2011**, *133*, 4718–4721.
5. Qi, Y.; Zhang, T.; Jing, C.; Liu, S.; Zhang, C.; Alvarez, P. J.; Chen, W. Nanocrystal facet modulation to enhance transferrin binding and cellular delivery. *Nat. Commun.* **2020**, *11*, 1–10.
6. Graf, C.; Nordmeyer, D.; Sengstock, C.; Ahlberg, S.; Diendorf, J.; Raabe, J.; Epple, M.; Köller, M.; Lademann, J.; Vogt, A.; Rancan, F.; Rühl, E. Shape-dependent dissolution and cellular uptake of silver nanoparticles. *Langmuir* **2018**, *34*, 1506–1519.
7. Nangia, S.; Sureshkumar, R. Effects of nanoparticle charge and shape anisotropy on translocation through cell membranes. *Langmuir* **2012**, *28*, 17666–17671.
8. Zhang, A.-Q.; Qian, D.-J.; Chen, M. Simulated optical properties of noble metallic nanopolyhedra with different shapes and structures. *Eur. Phys. J. D* **2013**, *67*, 231.
9. Wiley, B. J.; Im, S. H.; Li, Z.-Y.; McLellan, J.; Siekkinen, A.; Xia, Y. Maneuvering the Surface Plasmon Resonance of Silver Nanostructures through Shape-Controlled Synthesis. *J. Phys. Chem. B* **2006**, *32*, 15666–15675.

10. Gao, B.; Arya, G.; Tao, A. R. Self-orienting nanocubes for the assembly of plasmonic nanojunctions. *Nat. Nanotechnol.* **2012**, *7*, 433–437.
11. Gurunatha, K. L.; Marvi, S.; Arya, G.; Tao, A. R. Computationally Guided Assembly of Oriented Nanocubes by Modulating Grafted Polymer–Surface Interactions. *Nano Lett.* **2015**, *15*, 7377–7382.
12. Gao, M.; Zheng, X.; Khan, I.; Cai, H.; Lan, J.; Liu, J.; Wang, J.; Wu, J.; Huang, S.; Li, S.; Kang, J. Resonant light absorption and plasmon tunability of lateral triangular Au nanoprisms array. *Phys. Lett. A* **2019**, *383*, 125881.
13. Wang, Q.; Wang, Z.; Li, Z.; Xiao, J.; Shan, H.; Fang, Z.; Qi, L. Controlled growth and shape-directed self-assembly of gold nanoarrows. *Sci. Adv.* **2017**, *3*, e1701183.
14. Nagaoka, Y.; Tan, R.; Li, R.; Zhu, H.; Eggert, D.; Wu, Y. A.; Liu, Y.; Wang, Z.; Chen, O. Superstructures generated from truncated tetrahedral quantum dots. *Nature* **2018**, *561*, 378.
15. Gong, J.; Newman, R. S.; Engel, M.; Zhao, M.; Bian, F.; Glotzer, S. C.; Tang, Z. Shape-dependent ordering of gold nanocrystals into large-scale superlattices. *Nat. Commun.* **2017**, *8*, 14038.
16. Zhu, Y.; Xu, L.; Ma, W.; Xu, Z.; Kuang, H.; Wang, L.; Xu, C. A one-step homogeneous plasmonic circular dichroism detection of aqueous mercury ions using nucleic acid functionalized gold nanorods. *Chem. Commun.* **2012**, *48*, 11889–11891.
17. Ma, W.; Kuang, H.; Xu, L.; Ding, L.; Xu, C.; Wang, L.; Kotov, N. A. Attomolar DNA detection with chiral nanorod assemblies. *Nat. Commun.* **2013**, *4*, 1–8.
18. Lin, A.; Fu, S.-M.; Chung, Y.-K.; Lai, S.-y.; Tseng, C.-W. An optimized surface plasmon photovoltaic structure using energy transfer between discrete nano-particles. *Opt. Express* **2013**, *21*, A131–A145.

19. Kholmicheva, N.; Moroz, P.; Rijal, U.; Bastola, E.; Uprety, P.; Liyanage, G.; Razgoniaev, A.; Ostrowski, A. D.; Zamkov, M. Plasmonic nanocrystal solar cells utilizing strongly confined radiation. *ACS Nano* **2014**, *8*, 12549–12559.
20. Kagan, C. R.; Murray, C. B. Charge transport in strongly coupled quantum dot solids. *Nat. Nanotechnol.* **2015**, *10*, 1013.
21. Baumgardner, W. J.; Whitham, K.; Hanrath, T. Confined-but-connected quantum solids via controlled ligand displacement. *Nano Lett.* **2013**, *13*, 3225–3231.
22. Biggs, S.; Mulvaney, P. Measurement of the forces between gold surfaces in water by atomic force microscopy. *J. Chem. Phys.* **1994**, *100*, 8501–8505.
23. Argento, C.; French, R. Parametric tip model and force–distance relation for Hamaker constant determination from atomic force microscopy. *J. Appl. Phys.* **1996**, *80*, 6081–6090.
24. Lifshitz, E. The theory of molecular attractive forces between solids. *Sov. Phys. JETP* **1956**, *2*, 73–83.
25. Israelachvili, J. N. *Intermolecular and Surface Forces*; Academic press, 2015.
26. Hamaker, H. C. The London-van der Waals attraction between spherical particles. *Physica* **1937**, *4*, 1058–1072.
27. Tadmor, R. The London-van der Waals interaction energy between objects of various geometries. *J. Phys.: Condens. Matter* **2001**, *13*, L195.
28. Lee, B. H.; Arya, G. Orientational Phase Behavior of Polymer-Grafted Nanocubes. *Nanoscale* **2019**, *11*, 15939.
29. Takato, Y.; Benson, M. E.; Sen, S. Rich collision dynamics of soft and sticky crystalline nanoparticles: Numerical experiments. *Phys. Rev. E* **2015**, *92*, 032403.

30. Zhang, Z.; Horsch, M. A.; Lamm, M. H.; Glotzer, S. C. Tethered nano building blocks: Toward a conceptual framework for nanoparticle self-assembly. *Nano Lett.* **2003**, *3*, 1341–1346.
31. Tang, Z.; Zhang, Z.; Wang, Y.; Glotzer, S. C.; Kotov, N. A. Self-assembly of CdTe nanocrystals into free-floating sheets. *Science* **2006**, *314*, 274–278.
32. Damasceno, P. F.; Engel, M.; Glotzer, S. C. Predictive self-assembly of polyhedra into complex structures. *Science* **2012**, *337*, 453–457.
33. Teich, E. G.; van Anders, G.; Klotsa, D.; Dshemuchadse, J.; Glotzer, S. C. Clusters of polyhedra in spherical confinement. *Proc. Natl. Acad. Sci. U. S. A.* **2016**, *113*, E669–E678.
34. John, B. S.; Juhlin, C.; Escobedo, F. A. Phase behavior of colloidal hard perfect tetragonal parallelepipeds. *J. Chem. Phys.* **2008**, *128*, 044909.
35. Agarwal, U.; Escobedo, F. A. Mesophase behaviour of polyhedral particles. *Nat. Mater.* **2011**, *10*, 230.
36. Ilse, S. E.; Holm, C.; de Graaf, J. Surface roughness stabilizes the clustering of self-propelled triangles. *J. Chem. Phys.* **2016**, *145*, 134904.
37. Gilbert, E. G.; Johnson, D. W.; Keerthi, S. S. A fast procedure for computing the distance between complex objects in three-dimensional space. *IEEE J. Robotics and Automation* **1988**, *4*, 193–203.
38. Gottschalk, S.; Lin, M. C.; Manocha, D. OBBTree: A hierarchical structure for rapid interference detection. Proc. of ACM Siggraph'96. 1996; pp 171–180.
39. Ghaboussi, J.; Barbosa, R. Three-dimensional discrete element method for granular materials. *Int. J. Numer. Anal. Methods Geomech.* **1990**, *14*, 451–472.

40. Spellings, M.; Marson, R. L.; Anderson, J. A.; Glotzer, S. C. GPU accelerated Discrete Element Method (DEM) molecular dynamics for conservative, faceted particle simulations. *J. Comput. Phys.* **2017**, *334*, 460–467.
41. Trappe, V.; Prasad, V.; Cipelletti, L.; Segre, P.; Weitz, D. A. Jamming phase diagram for attractive particles. *Nature* **2001**, *411*, 772.
42. Lafitte, T.; Kumar, S. K.; Panagiotopoulos, A. Z. Self-assembly of polymer-grafted nanoparticles in thin films. *Soft Matter* **2014**, *10*, 786–794.
43. Allain, C.; Cloitre, M.; Wafra, M. Aggregation and sedimentation in colloidal suspensions. *Phys. Rev. Lett.* **1995**, *74*, 1478.
44. Tanaka, H.; Nishikawa, Y.; Koyama, T. Network-forming phase separation of colloidal suspensions. *J. Phys.: Condens. Matter* **2005**, *17*, L143.
45. Tang, T.-Y.; Zhou, Y.; Arya, G. Interfacial Assembly of Tunable Anisotropic Nanoparticle Architectures. *ACS Nano* **2019**, *13*, 4111–4123.
46. Weidman, M. C.; Smilgies, D.-M.; Tisdale, W. A. Kinetics of the self-assembly of nanocrystal superlattices measured by real-time in situ X-ray scattering. *Nat. Mater.* **2016**, *15*, 775.
47. Klinkova, A.; Thérien-Aubin, H.; Ahmed, A.; Nykypanchuk, D.; Choueiri, R. M.; Gagnon, B.; Muntyanu, A.; Gang, O.; Walker, G. C.; Kumacheva, E. Structural and optical properties of self-assembled chains of plasmonic nanocubes. *Nano Lett.* **2014**, *14*, 6314–6321.
48. O'Brien, M. N.; Girard, M.; Lin, H.-X.; Millan, J. A.; de la Cruz, M. O.; Lee, B.; Mirkin, C. A. Exploring the zone of anisotropy and broken symmetries in DNA-mediated nanoparticle crystallization. *Proc. Natl. Acad. Sci. U. S. A.* **2016**, *113*, 10485–10490.

49. Harper, E. S.; Waters, B.; Glotzer, S. C. Hierarchical self-assembly of hard cube derivatives. *Soft Matter* **2019**, *15*, 3733–3739.
50. Teich, E. G.; van Anders, G.; Klotsa, D.; Dshemuchadse, J.; Glotzer, S. C. Clusters of polyhedra in spherical confinement. *Proc. Natl. Acad. Sci. U. S. A.* **2016**, *113*, E669–E678.
51. Yang, M.; Sun, K.; Kotov, N. A. Formation and assembly- disassembly processes of ZnO hexagonal pyramids driven by dipolar and excluded volume interactions. *J. Am. Chem. Soc.* **2010**, *132*, 1860–1872.
52. Fang, Z.; Fan, L.; Lin, C.; Zhang, D.; Meixner, A. J.; Zhu, X. Plasmonic coupling of bow tie antennas with Ag nanowire. *Nano Lett.* **2011**, *11*, 1676–1680.
53. Kim, S.; Jin, J.; Kim, Y.-J.; Park, I.-Y.; Kim, Y.; Kim, S.-W. High-harmonic generation by resonant plasmon field enhancement. *Nature* **2008**, *453*, 757.
54. Sun, M.; Xu, L.; Bahng, J. H.; Kuang, H.; Alben, S.; Kotov, N. A.; Xu, C. Intracellular localization of nanoparticle dimers by chirality reversal. *Nat. Commun.* **2017**, *8*, 1847.
55. Auguié, B.; Alonso-Gómez, J. L.; Guerrero-Martínez, A.; Liz-Marzán, L. M. Fingers crossed: Optical activity of a chiral dimer of plasmonic nanorods. *J. Phys. Chem. Lett.* **2011**, *2*, 846–851.
56. vdWnano, <https://github.com/BrianHLeeProjects/vdWnano>.
57. Tang, T.-Y.; Arya, G. Anisotropic three-particle interactions between spherical polymer-grafted nanoparticles in a polymer matrix. *Macromolecules* **2017**, *50*, 1167–1183.
58. Pryamtisyn, V.; Ganesan, V.; Panagiotopoulos, A. Z.; Liu, H.; Kumar, S. K. Modeling the anisotropic self-assembly of spherical polymer-grafted nanoparticles. *J. Chem. Phys.* **2009**, *131*, 221102.

# Table of Contents Graphic

Analytical van der Waals interaction potential for faceted nanoparticles

Brian Hyun-jong Lee and Gaurav Arya

